Mesoscale eddy effects on the subduction of North Pacific mode waters

Lixiao Xu[1, 2*], Shang-Ping Xie[2, 1], Julie L. McClean[2], Qinyu Liu[1], and Hideharu Sasaki[3]

[1]Physical Oceanography Laboratory/ Qingdao Collaborative Innovation Center of Marine Science and Technology, Key Laboratory of Ocean-Atmosphere Interaction and Climate in Universities of Shandong, Ocean University of China, Qingdao, China

[2]Climate, Atmospheric Science and Physical Oceanography, Scripps Institution of Oceanography, University of California, San Diego, La Jolla, California

[3]Earth Simulator Center, JAMSTEC, Yokohama, Kanagawa, Japan

*Corresponding author: Lixiao Xu

Ocean University of China, 238 Songling Road, Qingdao, 266100, P. R. China

Email: xulixiao2004@126.com

Abstract

Mesoscale eddy effects on the subduction of North Pacific mode waters are investigated by comparing observations and ocean general circulation models where eddies are either parameterized or resolved. The eddy resolving models produce results closer to observations than the non-eddy resolving model. There are large discrepancies in subduction patterns between eddy resolving and non-eddy resolving models. In the non-eddy resolving model, subduction on a given isopycnal is limited to the cross point between the mixed layer depth (MLD) front and the outcrop line whereas in eddy resolving models and observations, subduction takes place in a broader, zonally elongated band within the deep mixed layer region. Mesoscale eddies significantly enhance the total subduction rate, helping create remarkable peaks in the volume histogram that correspond to North Pacific subtropical mode water (STMW) and central mode water (CMW). Eddy-enhanced subduction preferentially occurs south of the winter mean outcrop. With an anticyclonic eddy to the west and a cyclonic eddy to the east, the outcrop line meanders south, and the thermocline/MLD shoals eastward. As eddies propagate westward, the MLD shoals, shielding the water of low potential vorticity from the atmosphere. The southward eddy flow then carries the subducted water mass into the thermocline. The eddy subduction processes revealed here have important implications for designing field observations and improving models.

Keywords: Mesoscale eddy effects, subduction, mode waters, the North Pacific

1. Introduction

Mode waters, nearly vertically homogeneous layers within the main thermocline, are distinctive water masses commonly seen in the subtropical gyres of the world ocean [*Hanawa and Talley,* 2001]. Mode waters are believed to play an important role in climate variability. They memorize wintertime ocean-atmosphere interactions and re-emerge in the surface mixed layer in the subsequent winter season to interact with the overlying atmosphere [*Hanawa,* 1987; *Suga and Hanawa,* 1990; *Bingham,* 1992]. They determine the stratification within the main thermocline [*Kubokawa,* 1997] and regulate ocean biogeochemical cycles, for example, via the oceanic uptake of atmospheric CO_2 [*Bates et al.,* 2002].

A bias common to climate models in the North Pacific is that they simulate too much mode water [*Ladd and Thompson,* 2001; *Xie et al.,* 2011; *Xu et al*., 2012a, 2012b]. The potential vorticity (PV) minimum on isopycnals, a standard identifier of mode water, is too low in climate models relative to observational estimates. This biased signature persists downstream to the south whereas the observed PV minimum is much more diffused even before moving southward in the subtropical gyre [*Kobashi et al.*, 2006]. The overly large amount of simulated mode water may exaggerate mode water dynamics and affect the climate model's predictability. The present study compares North Pacific mode waters and subduction rates among observations and eddying and non-eddy resolving ocean general circulation models (OGCMs). In particular we investigate the role of mesoscale eddies in mode water subduction.

The effects of mesoscale eddies on mode water formation have received increasing attention over the past decade due to the concurrent increase of remotely sensed and in-situ observations [*Uehara et al.*, 2003; *Qiu et al.*, 2006, 2007; *Oka et al.*, 2009], and finer resolution OGCMs which resolve these processes [*Qu et al.*, 2002; *Nishikawa et al.*, 2010; *Oka and Qiu,* 2012]. *Marshall* [1997] suggested that in strong frontal regions where intense baroclinic instability occurs (e.g., in the Kuroshio Extension region), an ensemble of eddies provides advection via the "bolus velocity". This eddy advection term may enhance the subduction rate of mode waters by an amount of the same order as the mean flow subduction. Using the output of a global high-resolution OGCM, *Qu et al.* [2002] pointed out that mesoscale eddies enhance the annual subduction rate of North Pacific subtropical mode water (STMW) and central mode water (CMW) by up to 100 *m/yr*, or 34% of the total subduction. Recently, *Nishikawa et al.* [2010] estimated that eddies contribute some 50% of the total mode water subduction rate based on an eddy resolving OGCM ($1/12^{o}\times 1/18^{o}$) simulation of the western North Pacific. From a climatological viewpoint, subduction is limited to the intersections of the winter mixed layer depth (MLD) front and outcrop lines [*Xie et al.*, 2000], but eddies may broaden the horizontal extent of the subduction sites. Using Argo profiling float data, *Oka and Suga* [2003, 2005] found that the STMW formation region extends as far east as 175°E, while the CMW extends as far west as 155°E. Remarkably, *Oka et al*. [2009] observed newly formed CMW in the western North Pacific (27.5°N, 145°E) in a high-density hydrographic survey. How eddies broaden the subduction zone has not been studied systematically.

Several physical processes of eddy subduction and transport have been identified. Anticyclonic eddies in deep mixed layers have been found to contribute substantially to STMW formation and transport [*Uehara et al.*, 2003; *Pan and Liu,* 2005]. Combined analyses of satellite-derived sea surface height (SSH) anomalies and Argo profiling float data suggest that STMW tends to be trapped and transported by anticyclonic eddies [*Kouketsu et al.*, 2011; *Liu and Li*, 2013]. Based on high-resolution OGCM results, *Nishikawa et al.* [2010] suggested two local processes as possible causes of eddy subduction: destruction of a horizontal PV gradient by eddy mixing, and the southward translation of anticyclonic eddies that carry low PV. Other processes such as the eddy-induced meandering of surface outcrops might also play an important role in eddy subduction. As illustrated schematically in Fig. 1, net subduction can be finite even when the Eulerian-mean subduction is zero if eddies cause the outcrop lines of an isopycnal layer to open more widely during a subduction period than during an obduction period [see also *Marshall*, 1997; *Kwon et al.*, 2013]. Therefore, when evaluating the net contribution of eddies, the meandering of surface density outcrops should be taken into consideration.

The present study investigates eddy effects on the subduction of North Pacific mode waters (i.e. STMW and CMW). We wish to address the following questions: does the representation of mode water subduction differ among observations and eddy resolving and non-eddy resolving models? If yes, how do eddies cause these differences? What are the physical processes responsible for eddy subduction? We show that there are large differences in the subduction patterns between eddy resolving and non-eddy resolving models. Eddies significantly enhance the total subduction rate, and broaden the subduction zone within the deep mixed layer region. We find that eddy subduction on isopycnals preferentially occurs south of the winter mean outcrop line. The eddy subduction takes place on the eastern (western) flank of the anticyclonic (cyclonic) eddies, where the outcrop line meanders south and the mixed layer shoals eastward. The newly formed mode waters are sheltered from the surface by the shoaling MLD, and are advected to the south by the eddy flow between the anticyclonic and cyclonic eddies. The paper describes and provides evidence for these eddy subduction processes.

The rest of this paper is organized as follows. Section 2 briefly describes the models and data used in this study. Section 3 compares the mean fields related to mode water subduction as represented by eddy resolving and non-eddy resolving models and observations. Section 4 investigates key mechanisms of eddy subduction. In section 5 we provide a summary.

2. Data and Methods

2.1 Observations

A fundamental aspect of this study is the comparison of observational and simulated quantities to gauge the relative veracity of the simulations. Mean SSH was obtained from the CNES-CLS09 product of *Rio et al.* [2011] at a spatial resolution of 1/4°, while weekly SSH anomaly (SSHA) for 1994-2007 came from the Archiving, Validation, and Interpretation of Satellite Oceanographic (AVISO) data [*AVISO*, 2008] whose horizontal resolution is 1/3°; we further re-gridded the fields to a 1/4° grid. Monthly net surface heat flux data for 1994-2007, on a 1/3° latitude × 1.0° longitude grid, was acquired from the Global Ocean Data Assimilation System (GODAS, http://www.esrl.noaa.gov/psd/) developed at the National Centers for Environmental Prediction (NCEP). Salinity and potential temperature were obtained from the 1° gridded monthly Roemmich-Gilson Argo Climatology constructed from Argo float data for the period 2004-2013 [*Roemmich and Gilson*, 2009].

2.2 The Ocean Model for the Earth Simulator (OFES)

The OGCM for the Earth Simulator (OFES) is based on the third Modular Ocean Model (MOM3), which was substantially modified for optimal performance on the Earth Simulator. The model domain extends from 75°S to 75°N, with a horizontal grid spacing of 1/10°. The vertical spacing varies from 5 *m* at the surface to 330 *m* at the maximum depth of 6,065 *m*. There are 54 vertical levels. The model was spun up for 50-years using National Centers for Environmental Prediction and the National Center for Atmospheric Research (NCEP/NCAR) monthly mean atmospheric reanalysis fluxes. Subsequently, it was driven by daily mean NCEP/NCAR wind stresses and surface heat fluxes for the period from 1950 to 2010. Scale-selective damping by a biharmonic operator is utilized for horizontal mixing of momentum and tracers to suppress computational noise. The viscosity and diffusivity coefficients are -2.7×10^{10} m^4 s^{-1} for momentum and -9×10^{9} m^4 s^{-1} for tracers at the equator. They vary proportionally to the cube of the zonal grid spacing. The vertical viscosity and diffusivity are calculated using the K-profile parameterization (KPP) [*Large et al.*, 1994]. Further details of the model and the simulation can be found in *Sasaki et al.* [2008] and *Taguchi et al.* [2007]. The 3-day model outputs are downloaded from the Asia Pacific Data Research Center (http://apdrc.soest.hawaii.edu/datadoc/ofes/ofes.php).

2.3 The Parallel Ocean Program (POP)

a. High-Resolution (POPH)

A nominal 1/10°, 42-level global configuration of the Los Alamos National Laboratory (LANL) Parallel Ocean Program was configured on a tripolar grid. The horizontal grid spacing at the equator is 0.1°, with the latitudinal spacing decreasing with cosine (latitude). The vertical levels are smoothly varying in thickness from 10 *m* at the surface to 250 *m* at the maximum depth of ~6,000 *m*. The model was initialized from year 30 of a century-long simulation carried out by *Maltrud et al.* [2010] using this same configuration, except that it was forced with monthly-averaged "Normal Year (NY)" Coordinated Ocean-Ice Reference Experiments (CORE) atmospheric fluxes constructed by *Large and Yeager* [2009]. The simulation analyzed here was forced with CORE Phase 2 (CORE2) interannually varying forcing (IAF) for 1990-

2007. The first three years of the simulation were considered an adjustment period to the high frequency forcing. The subgrid scale horizontal mixing was parameterized using biharmonic operators for momentum and tracers. The viscosity and diffusivity values vary spatially with the cube of the averaged grid length for a given cell and have equatorial values, denoted by the subscript 0, of ν_0= -2.7×10^{10} m^4 s^{-1} and κ_0 = -0.3×10^{10} m^4 s^{-1}. The vertical mixing was based on KPP. We extracted the daily-averaged output in the subtropical North Pacific region (10°N-50°N, 110°E-110°W) for this study where the horizontal grid resolution is around 8 *km*.

b. Low-Resolution (POPL)

A non-eddy resolving POP simulation with a nominal horizontal resolution of 1° was carried out for comparative purposes with the high-resolution ocean simulations. The low-resolution model was first spun up from rest for 30 years using CORE NY forcing; it was then forced with CORE2 IAF for 1990-2007. The *Gent and McWilliams* [1990] parameterization for eddy-induced tracer transport was used with isopycnal and thickness diffusion coefficients of 600 m^2 s^{-1}. This value was chosen to be low to highlight the effects of resolved eddies on mode water formation and circulation when comparing the eddy resolving (OFES and POPH) and non-eddy resolving (POPL) simulations. Submesoscale mixing was not active. The other parameterization choices were identical to those used to configure POP in the Community Climate System Model 4 (CCSM4) simulations [*Danabasoglu et al.*, 2012].

2.4 Data Processing

Results based on AVISO observations and output from the three simulations are compared for the period 1994 to 2007. Argo observations, however, are only available from 2000 to 2013. To understand if results obtained from this shorter period Argo data would bias our interpretations we compared results from the models and Argo for their overlapping period 2000-2007. We consider that the inconsistency between the time periods of the eddy resolving simulations and observations will not cause large discrepancies in the mean features of mode water subduction.

Three-daily fields are used from POPH and OFES; the OFES fields are snapshots whereas the POPH fields are daily-averages. Our study considers variability on much longer time scales so our results will not be significantly affected by this difference. To provide further support for this choice, we also compared snapshot and daily averaged fields, including potential density and velocities, from the Kuroshio Extension Observatory (KEO) buoy [*Cronin et al.*, 2008], located to the south of the Kuroshio Extension current at 32.3°N, 144.6°E. The difference between the snapshot and daily-averaged fields is relatively small: it accounts for only ~3.9 % of the total variance. Therefore, the calculated results should be independent of the different archiving methods used for POPH and OFES.

At a single station/grid point without information from its surroundings, data should cover at least several eddy life cycles to produce a statistically reliable mean field. Given that the mesoscale eddies in the subtropical North Pacific have a typical timescale of 100-200 days [e.g., *Ebuchi and Hanawa, 2000*], the 14-year time series of data and model output used in this study is long enough for this purpose. Following *Smith et al.* [2000], we estimated the first baroclinic Rossby radius for OFES and POPH, which is mostly >10 *km* in the subtropical North Pacific region (not shown). Typical length scales for mesoscale eddies are linearly related to the Rossby radius but are somewhat larger [*Smith et al.*, 2000], so the mesoscale eddies should be reasonably well resolved in the study region in OFES (uniform 0.1° resolution) and POPH (8 *km* in the study domain).

3. Comparison of the mean fields

With resolved eddies in the high-resolution models and observations, mean fields such as SSH, MLD and PV may differ from those in the non-eddy resolving model. In order to examine the eddy effects on the large-scale climatology, this section compares the 1994-2007 mean fields related to mode water subduction among observations, OFES, POPH and POPL.

3.1 Sea Surface Height

Figure 2 depicts the mean and standard deviation of SSH in the study region from model simulations and observations. The observed mean SSH was taken from *Rio et al.* [2011] and the variance was calculated from the AVISO altimetry data. The geostrophic relation directly relates geostrophic currents at the ocean surface to the horizontal gradient of SSH. Compared to observations, the separation latitude (very close to 34 ^{o} N) of the Kuroshio current and the structure of the Kuroshio Extension (KE) jet are effectively reproduced in the eddy resolving models (i.e., OFES and POPH), whereas a northward overshooting Kuroshio appears in POPL, a feature common to other non-eddy resolving models [*Guo et al.*, 2003]. The intensity of the eddy field can be assessed by comparing the simulated and observed standard deviation of the SSH variability. In eddy resolving models, the variability and eddy activity in the Kuroshio Extension region are comparable to those of observations with a magnitude of ~30 *cm*, even though the eddy activity in OFES is larger than in POPH, especially north of the KE around 42 ^{o} N. By contrast, the non-eddy resolving model shows very low variability in the KE region. Just prior to separating from the coast of Japan, the Kuroshio in the OFES field shows a deep meander; this feature is not seen in AVISO or POPH. However, its effect on STMW and CMW subduction is considered to be small because its location is far from the STMW and CMW subduction regions.

3.2 Mixed Layer Depth

The mixed layer depth (MLD) is defined as the depth at which potential density is different from the sea surface (10 *m*) density by 0.03 kg/m^3. This simple definition has been adopted by numerous previous studies [e.g., *Huang and Qiu*, 1994; *Suga et al.*, 2004]. We have confirmed that the resulting MLD was not particularly sensitive to a threshold ranging from 0.01 to 0.125 kg/m^3. The MLD reaches its annual maximum in March (Fig. 3). There are two MLD maxima deeper than 150 *m* along 32°N and 42°N in the gridded Argo Data (Fig. 3a). The northern band of deep MLD extends to 165°W and is associated with CMW, while the southern band extends to 165°E and is associated with STMW [*Suga et al.*, 2004]. Sandwiched in between is a shallower mixed layer along the KE jet, extending from the western boundary to 165°W. The two eddy resolving models, OFES and POPH, could only reproduce this "sandwiched-structure" well in the upstream region of the KE (west of 160°E), where the strong KE jet exists (Fig. 3b, c). In the downstream region of the KE jet (east of 170°E), the deep MLD in OFES and POPH becomes a single wide pool, whereas the deep MLD (>150 *m*) in observations is confined to north of 37°N. In POPL, there is only one single deep mixed layer pool, with a sharp MLD front slanted northeastward on the southern flank (Fig. 3d). The MLD in POPH and OFES in the downstream KE, more closely matches the distribution of the non-eddy resolving model, POPL, than the observations. The cause of the model bias in MLD in the downstream portion of the KE is beyond the scope of this study, but it might be associated with surface heat flux biases (Fig. 4); the patterns of March mean net surface heat flux from the models are somewhat correlated with the model MLD distributions.

3.3 Potential Vorticity

The PV distribution on the core layers of STMW and CMW from Argo, OFES, POPH and POPL are seen in Fig. 5. The PV (Q) is calculated by

$$Q = -\frac{f}{\rho_0}\frac{\partial \rho}{\partial z} \ . \tag{1}$$

Here ρ is potential density, f is the Coriolis parameter, and ρ_0 is a reference density (1024 kg/m^3). The acceleration potential relative to 2000 *db* is superimposed, approximating the streamfunction on isopycnal surfaces. The core layer of STMW or CMW is inferred from the total volume of the low PV water ($< 1.5 \times 10^{-10}\ m^{-1}\ s^{-1}$) for the density class (Table 1 and the red curves of Fig. 8) over the North Pacific (120°E-140°W; 20°-40°N).

In the non-eddy resolving model POPL, the MLD front slants northeastward from the southwestern region of the subtropical gyre, whereas the outcrop lines slant southeastward due to the northward overshooting Kuroshio on the Japanese coast (Fig. 3d). Mode water with minimum PV forms where the outcrop line intersects the MLD front between 30°N and 34°N (Figs. 5g-h, 6d) by lateral induction [*Xie et al.,* 2000]; the mode water (i.e., STMW or CMW) formation is limited to a narrow region, so narrow that we call it the subduction point (Fig. 5 bottom panels). In observations (Fig. 3a), the MLD gradient is weak and the outcrop lines are almost zonal and nearly in parallel with the MLD front, due to the jet and eddy effects. Mode water is formed in a broader zone along the outcrop line; the STMW and CMW formation is even found north of the MLD front (i.e., within the deep MLD region), implying that eddies are broadening the subduction zone. In the eddy-resolving models, the MLD front is stronger than in observations but is still weaker than in POPL, while the outcrop lines slant slightly southeastward, intersecting the MLD front to the east of

165°E (Fig. 3b-c). Similar to observations, mode water is formed in a broader region along the outcrop line.

Figure 6 shows zonal mean sections of potential density, MLD, and PV between 140° and 180°E for observations, OFES, POPH, and POPL. In the eddy resolving models and observations (Fig. 6a-c), the vertical PV minimum is concentrated in a narrow density range (i.e., 25.2-25.4 σ_θ for observations, 25.2-25.6 σ_θ for OFES and 25.0-25.4 σ_θ for POPH), whereas in POPL, the vertical PV minimum is found in a wide density range of 25.3-26.0 σ_θ (Fig. 6d). PV dissipation along the mean trajectory of the low PV tongue for the core layers of both STMW and CMW shows that downstream of the formation site the PV minimum persists over a long distance in POPL whereas it decays rapidly near the subduction site in the eddy-resolving models and observations (Fig. 7), illustrating the strong dissipative role of mesoscale eddies. The comparison of major features related to mode water subduction reveals large differences between the eddy resolving and non-eddy resolving models. Due to the jet and eddy effects, mode waters in the eddy-resolving simulations are formed in a broader horizontal zone along the outcrop line, and the PV minimum tends to be confined to narrow density ranges near the formation region. In the next section, we investigate key mechanisms for eddy subduction.

4. Subduction Rate

This section investigates the effects of mesoscale eddies by diagnosing the subduction rate from the models and observations. Section 4.1 gives the physical basis for how explicitly resolved mesoscale eddies contribute to the total subduction of a water mass, and section 4.2 quantifies the eddy subduction. Section 4.3 investigates the possible mechanisms of eddy subduction. Section 4.4 depicts the eddy subduction patterns by tracing the water parcels released at the base of the March mixed layer to calculate the effective annual subduction rate.

4.1 Physical Basis for Analysis

According to *Cushman-Roisin* [1987] and *Williams* [1989, 1991], the subduction rate, S, is the volume flux of fluid per unit area entering the thermocline from the mixed layer:

$$S = -\left(\frac{\partial h}{\partial t} + \mathbf{u}_h \cdot \nabla h + w_h\right) . \tag{2}$$

The subduction rate increases either through increasing the downward velocity at the base of the mixed layer, w_h, the rate of mixed-layer shallowing, $\partial h / \partial t$, or the horizontal advection of fluid out of the mixed layer, $\mathbf{u}_h \cdot \nabla h$, where h is the thickness of the mixed layer. To quantify the net contribution of eddies to the total subduction, however, a simple Eulerian time-average of Eq. 2 is not appropriate since the surface area over which the water mass is outcropped is itself evolving [*Marshall,* 1997, see also Fig. 1]. Adapted from *Marshall* [1997], the net subduction of water mass (M) of a density range $\sigma_1 \leqslant \sigma < \sigma_2$ is given by the local subduction rate S(t) multiplied by spacing, ΔA(t), between the two bounding outcrops, σ_1 and σ_2: $M = S(t)\Delta A(t)$.

Separating the fluid variables into "mean" and "eddy" components (e.g., $h = \overline{h} + h'$, $\mathbf{u}_h = \overline{\mathbf{u}_h} + \mathbf{u}_h'$), where the "mean" represents a low-pass time-filtering operation over several baroclinic eddy life cycles, one finds

$$\overline{M} = \overline{S(t)\Delta A(t)} = \{\overline{\mathbf{u}_h} \cdot \nabla\overline{h} + \overline{w_h}\}\overline{\Delta A} + \overline{\{\mathbf{u}_h'\nabla h'\}}\overline{\Delta A} + \overline{\{\frac{\partial h}{\partial t} + \mathbf{u}_h \cdot \nabla h + w_h\}'\Delta A'} . \tag{3}$$

The eddy subduction is defined as the second and third terms of the right-hand side of Eq. 3. Here $\overline{\Delta A}$ is the outcrop area between time-mean outcrop lines for σ_1 and σ_2, and $\Delta A'$ represents the transient deviations from the time mean. While the MLD change term $\frac{\partial h}{\partial t}$ vanishes over an annual cycle from the Eulerian viewpoint, its correlation with the spacing of the meandering density outcrops, $\overline{\frac{\partial h'}{\partial t}\Delta A'}^{\sigma}$, causes large contributions to the total subduction, as shall be shown in subsection 4.3. Hereafter we use the bar sigma notation for the isopycnal average. The relationship between the potential vorticity (Q) of water subducted at the base of the mixed layer and the net subduction of water mass (M) is discussed in the Appendix.

4.2 Eddy Subduction

The water mass subduction, $\bar{M}$, illustrates the importance of eddies in the overall mass subduction from the mixed layer into the thermocline. However, Eq. 3 is not ideal for diagnosing eddy subduction. In this subsection, we develop a more practical expression. The annual subduction M of a density range ($\sigma_1 \leqslant \sigma < \sigma_2$), following the time-dependent, meandering surface density outcrops, can be written as

$$\overline{M(\sigma_1 \le \sigma < \sigma_2)} = \frac{1}{T}\int_0^T [\sum_{\sigma_1 \le \sigma < \sigma_2} S_{i,j}(t) \cdot \Delta A_{i,j}]dt, \qquad (4)$$

where (i, j) is the horizontal grid index in the zonal and meridional directions in the calculation domain (135°E-155°W, 25°-45°N), $\Delta A_{i,j}$ is the area of the horizontal grid box that falls within the surface density range, t is time, and T is the averaging period. Similar to *Nishikawa et al.* [2010], we introduce three components of subduction:

- Total subduction M_{total}, calculated from the high-frequency output for 14 years (10 years from Argo);
- Mean subduction M_{mean}, calculated from monthly mean fields; and
- Eddy subduction M_{eddy}, the difference between the total and mean (i.e., $M_{eddy} = M_{total} - M_{mean}$).

Figure 8 shows the subduction and its components (M_{mean}, and M_{eddy}) at 0.1 σ_θ intervals for observations, OFES, POPH, and POPL. For observations, the geostrophic velocities were calculated from Argo hydrographic data [*Huang and Qiu*, 1994]. Eddy effects may be smoothed out in the observational result due to the use of the 1°×1° gridded Argo data. M_{eddy} for the non-eddy resolving model is due to weak sub-monthly disturbances from the monthly mean fields, and does not represent mesoscale eddy effects. Table 1 summarizes the total subduction and its components for STMW and CMW. These results are generally consistent with the results from *Tsujino and Yasuda* [2004], and *Nishikawa et al.* [2010], albeit with a slightly different study region. As in previous studies, eddies significantly increase the subduction of STMW and CMW.

The total subduction has two marked peaks in both the observations and the eddy resolving models (OFES and POPH). The lighter density one corresponds to STMW, while the denser represents CMW. In comparison, a single broad peak appears in the CMW range in POPL (Fig. 8j). As discussed in the last section, maximum subduction occurs where the outcrop line intersects the MLD front in the non-eddy resolving model [*Xie et al.*, 2011]. Together with the northeastward slanted MLD front and the southeastward slanted outcrop lines, large subduction (PV minimum) is almost equally distributed in a broad density range (i.e., 25.3-26.4 σ_θ). By contrast, in the eddy resolving models and observations, the MLD gradient is weaker and the outcrop lines tend to be in parallel with the MLD front, due to jet and eddy effects. Subduction is concentrated in narrow density ranges (Fig. 8 a, d, g) corresponding to those of the two deep MLD bands (Fig. 3 a-c; Fig. 5 a-f). The mean subduction (M_{mean}) peaks for STMW and CMW are present in observations and the eddy resolving models, but have lower magnitudes. In contrast, the eddy subduction, M_{eddy}, is larger than M_{mean} with distinct peaks in the observations and OFES and POPH, implying important physical mechanisms for mode water subduction due to eddies.

4.3 Physical processes

The eddy effects on the subduction of STMW and CMW are quantified in the preceding subsection. This subsection identifies the physical processes of eddy subduction using the OFES 3-day outputs in the core layer of STMW (25.3 σ_θ). We choose the STMW layer for our study because the largest eddy subduction (10.33 *Sv*, ~80% of the total subduction) occurs there, and because of good agreement with observations regarding the simulation of STMW. The core STMW layer for our analysis is 25.3 ±0.05 σ_θ. We only diagnose subduction in March, the time of the year when the mixed layer is deepest and subduction is strong.

Figure 9a shows the outcrop frequency of the 25.3 ±0.05 σ_θ layer based on the OFES 3-day outputs in March from 1994 to 2007. The time-varying outcrop includes big meanders. The isopycnal subduction rate and its components are shown in Fig. 9b-e. The *isopycnal subduction rate*, $\overline{S}^{\sigma}$, is obtained by integrating the time-varying subduction rate (Eq. 2) within the density range of 25.25 ≤σ<25.35

$$\overline{S}^{\sigma} = \frac{\frac{1}{T}\int_0^T S_{i,j}(t)\cdot \Delta A_{i,j}\Big|_{25.25\le\sigma<25.35} dt}{\frac{1}{T}\int_0^T \Delta A_{i,j}\Big|_{25.25\le\sigma<25.35} dt}. \qquad (5)$$

The superscript σ indicates that it is average for a given isopycnal layer, distinct from the simple Eulerian mean S. The time integration here is based on the OFES 3-day outputs in March for 14 years. The isopycnal subduction rate is decomposed into

$$\overline{S}^{\sigma} = \overline{\frac{\partial h}{\partial t}}^{\sigma} + \overline{\mathbf{u}_h \cdot \nabla h}^{\sigma} + \overline{w_h}^{\sigma}. \qquad (6)$$

The concept of the downward transport of $\overline{S}^{\sigma}$ and its components is analogous to the eddy bolus transport or the eddy thickness transport [*Marshall,* 1997; *Kwon et al,* 2003], which refers to the transport caused by the subgrid-scale correlation between the velocity of water mass and the thickness of isopycnal.

As shown in the last subsection, eddy subduction dominates the total subduction on 25.3 σ_0 in OFES. There is a broad eddy subduction zone extending from 140°E to almost 160°W, within the region of the deep mixed layer (Fig. 9b). The maximum eddy subduction takes place south of the mean 25.3 σ_0 outcrop, dominated by the MLD tendency term (Fig. 9c-e), $\overline{\frac{\partial h}{\partial t}}^{\sigma}$, due to the cross-correlation between the temporal variations in MLD and outcrop area. From a Eulerian point of view, the STMW and lighter CMW are formed in the case of large lateral induction by the mean flow [*Suga et al.,* 2008], $U_h \cdot \nabla h$, roughly at the intersection of the outcrop and MLD front in climate models [*Xie et al.*, 2000]. However, in an eddying ocean, the STMW and CMW are formed within the deep MLD region and to the south of the mean outcrop line (Fig. 9b), implying very different physical mechanisms. The isopycnal subduction rate $\overline{S}^{\sigma}$ peaks well south of the mean outcrop because eddy subduction is associated with the southward meanders of the outcrop line. In other words, immediately south of the mean outcrop, the isopycnal is occasionally exposed to the atmosphere by eddies. There, the STMW layer is not always shielded from the mixed layer as the climatology implies, but may be exposed to the mixed layer in the presence of eddies. The mixed layer waters are injected into the pycnocline as the mixed layer shoals in time in an expanded outcrop area, expressed as the $\overline{\frac{\partial h}{\partial t}}^{\sigma}$ term.

Similar results are also obtained on other isopycnals, including both the STMW and CMW layers for OFES and POPH (not shown here). Along a similar line, *Kwon et al.* [2013] showed that the "seasonal eddy subduction", due primarily to subannual correlations between the MLD and the outcrop area, contributed to mode water subduction in the Southern Ocean. They suggested that the eddy contribution is a key component of the "seasonal eddy subduction", compared with the seasonal perturbations. Besides the eddy effects, surface outcrops also change their locations on seasonal to interannual timescales. Here the seasonal variation is eliminated since we only focus on subduction in March, while POPL results suggest that interannual variability in the winter outcrop is not the major cause of large subduction in mode-water density ranges (Fig. 8i).

To determine how mode water is subducted by eddies, a snapshot from OFES on March 26th, 2000 is shown in Fig. 10. The deep mixed layer occurs preferentially in anticyclonic eddies and the recirculation gyre. The mixed layer is relatively shallow in cyclonic eddies at the troughs of the meandering jet (Fig. 10a, b). The instantaneous outcrop area (hatched pattern in Fig. 10b) for the density range of 25.25~25.35 σ_θ intrudes to the south on the eastern flank of the anticyclonic eddies (e.g., 145^{o}E), and is even found isolated inside anticyclonic eddies (e.g., 143.5^{o}E). Low PV water forms where the outcrop area meanders to the south (Fig. 10c), with major subduction events taking place around 144^{o}E and 151^{o}E, 33^{o}N on the eastern flank of anticyclonic eddies. The three components of instantaneous subduction rate (RHS of Eq. 2) are shown in the right hand panels of Fig. 10. The newly formed low PV water is generally co-located with the MLD tendency term $\frac{\partial h}{\partial t}$, while it has little to do with the lateral induction and vertical pumping terms.

To generalize these findings, we make composites (Figs. 11-12) of the eddy subduction terms for the isopycnal layer 25.25~25.35 σ_θ based on the OFES 3-day outputs in March from 1994 to 2007. The center locations for the composite are determined when the total isopycnal subduction rate (Fig. 9b) exceeds 4.0×10^{-5} m/s. For each case meeting this criterion, a square region (5° latitude by 7° longitude), centered at the site of maximum isopycnal subduction, is extracted. Then all of these maps (626 cases) are averaged centered at the maximum isopycnal subduction. The statistical significance of the composite is evaluated using a t-test.

Figure 11 shows the horizontal composite maps. Consistent with the snapshot (Fig. 10), the eddy subduction takes place between the anticyclonic and cyclonic eddies, where the southward dense (cold) advection takes place (Fig. 11a). The maximum outcrop area anomalies are collocated with the temporal shoaling of the MLD as the eddy pair with an eastward shoaling thermocline propagates westward (Fig. 12a-b). The mixed layer water is soon to be sheltered from the surface as the MLD shoals in time, forming the mode water. Results from Figs. 10 and 11 suggest that the correlation between the MLD tendency term and the meandering density outcrops, i.e., $\overline{\frac{\partial h'}{\partial t}\Delta A'}^{\sigma}$, is the dominant mechanism for eddy subduction. The center of the composite is displaced south of the winter mean outcrop latitude by 1.8° (Fig. 9b). This corresponds to an increase of the isopycnal outcropping in southern meanders of the instantaneous outcrop line, giving rise to a cross-correlation between the increased outcrop area and temporal shoaling of the MLD. By contrast, the contributions from the lateral induction and the vertical pumping terms are small for isopycnal subduction (Fig. 11 e-f).

Figure 12 displays vertical transects of the composite. The deep mixed layer is often accompanied by a deep thermocline in anticyclonic eddies in the North Pacific, and vice versa [*Suga and Hanawa*, 1990; *Uehara et al.*, 2003]. Eddy-induced thermocline displacements are much larger than the gyre-scale spatial variations of the thermocline depth. The potential temperature is warmer and the density is lighter in anticyclonic eddies relative to cyclonic eddies. The 25.25 σ_θ isopycnal is outcropped between the anticyclonic and cyclonic eddies, well south of its mean outcropping due to the dense (cold) advection. Three days later, the MLD becomes stratified partly due to the surface heating anomaly (Fig. 11b, c; Fig. 12a), and the 25.25 σ_θ isopycnal is no longer outcropped (red curves in Fig. 12a), sheltered under the shoaling MLD as eddies travel westward. Both the surface heating anomaly and the west propagation of eddies are responsible for the MLD shoaling, sequestering low PV waters from the surface. After subduction, the newly formed mode waters are advected to the south beneath the mixed layer by the southward flow between the anticyclonic and cyclonic eddies (Fig. 12b, d). Being injected into the thermocline south of the March mean outcrop region, the water mass tends to stay in the thermocline, rather than being entrained into the mixed layer. Thus, the effect of the southward eddy flow that advects the subducted water parcels is not balanced by the effect of the northward eddy flow [*Qu et al.*, 2002]. The next subsection illustrates this eddy subduction effect by tracing water parcels at the base of the March mixed layer for one year to calculate the effective annual subduction rate.

4.4 Annual Subduction Rate

To obtain a geographic distribution of eddy effects on the subduction, the annual subduction rate is calculated by integrating the instantaneous subduction rate (Eq. 2) over one year from the end of the first winter t_1 to that of the second winter t_2 in Lagrangian coordinates [*Qiu and Huang,* 1995]:

$$S_{ann} = \frac{1}{T}\int_{t_1}^{t_2} S(t)dt = -\frac{1}{T}\int_{t_1}^{t_2} w_h dt + \frac{1}{T}(h(t_1) - h(t_2)) \ , \qquad (7)$$

where T = 1 *yr*. The first term on the right hand side represents the vertical pumping at the base of the mixed layer averaged along the Lagrangian trajectory, and the second term the contribution from temporal/lateral induction due to the sloping mixed layer base. In the following, we trace water parcels released at the base of the March mixed layer using three-daily fields to examine the eddy contribution. The total subduction rate, S_{total}, is calculated using the instantaneous model outputs, while the mean subduction rate, S_{mean}, is calculated using monthly mean fields. The eddy-induced subduction rate, S_{eddy}, is measured simply as the difference between S_{total} and S_{mean}, following *Qu et al.* [2002].

The annual subduction rate and its components are shown in Fig. 13. The eddy subduction, $S_{eddy,}$ is as large, and perhaps larger than the subduction by the mean flow. The spatial distributions of the eddy and mean flow subduction are different: eddy subduction happens in a broader zone (mostly inside the deep mixed layer region), whereas strong subduction by the mean flow is concentrated along the MLD front as in POPL, implying the importance of lateral induction for the latter. These features are consistent with the mode water formation patterns discussed in the preceding section. The mode water formation transforms from a narrow subduction point in non-eddy resolving POPL, to a broader subduction zone in the eddy-resolving simulations due to the strong eddy subduction processes.

In this section, we have diagnosed the subduction rate in three different ways to investigate the direct eddy effects. We find that eddies significantly increase the subduction rate, and expand the subduction region inside the deep mixed layer. South of the March mean outcrop line the isopycnal is occasionally exposed to the atmosphere by eddies in southward meanders of the outcrop line. That is the time when strong subduction happens via the MLD shoaling.

5. Summary

We have investigated the role of eddies on the subduction of North Pacific mode waters based on a comparison of observations and two eddy resolving OGCMs and one non-eddy resolving OGCM. Subduction differs greatly between eddy resolving and non-eddy resolving models. In the non-eddy resolving model, subduction on a given isopycnal is concentrated at the intersection of the MLD front and the outcrop, so narrow that it may be called subduction point. In eddy resolving models and observations, by contrast, subduction takes place in a broader zone, inside the region of deep MLD. The March mean MLD front, which is a narrow transition zone separating shallow and deep mixed layers, is less pronounced in eddy resolving models than in the non-eddy resolving model. The realistic separation of the Kuroshio from the Japanese coast and the strong Kuroshio Extension jet make outcrop lines tend to be zonal in the eddy resolving models. Both of these effects allow subduction to occur in a broader zone. In addition to widening the subduction region, eddies significantly increase the total subduction rate. Strong eddy subduction takes place in the deep mixed layer region in contrast to the non-eddy resolving model where subduction by the mean flow is confined to the MLD front.

A key finding of our study is that eddy subduction takes place south of the mean winter outcrop line between an anticyclonic eddy with a deep mixed layer to the west and a cyclonic eddy with a shallow mixed layer to the east (Fig. 14). There, the eddy pair causes the outcrop line to meander southward by dense (cold) advection, and the

MLD shoals with time via surface heating anomaly and the west propagation of eddies. The cross-correlation between the temporal shoaling of the mixed layer and southward migration of the outcrop line intensifies subduction. Advected by the southward flow between the anticyclonic and cyclonic eddies, the subducted water mass moves southward beneath the upper thermocline.

Substantial differences exist in the North Pacific mode water simulation between eddy resolving and non-eddy resolving models. Further work, however, needs to be done to realistically simulate MLD in eddy-resolving models. We note that the MLD in eddy resolving models is much deeper than in observations. Specifically in the eastern part of the Kuroshio Extension, eddy resolving and non-eddy resolving models share a common deficiency: the winter mixed layer is too deep, forming a broad pool of deep MLD instead of a narrow deep MLD band north of the KE jet in observations. This deficiency in MLD simulation is likely to affect CMW formation.

Our results indicate that eddies significantly increase the total subduction rate, by up to 50%. However, the mode waters are dissipated quickly after being subducted into the thermocline (Figs. 5-7), not conforming to the key assumption of PV conservation in ventilated thermocline theories. In non-eddy resolving models, isopycnal PV dissipates too slowly along the low PV tongues of the core layers of STMW and CMW. Such non-conservative properties of mode water PV in observations and eddy resolving models have important implications in regard to their effects on the North Pacific subtropical countercurrent (*Kubokawa,* 1997; *Kobashi et al.,* 2006; *Xu et al.,* 2012b) and ocean stratification in general. Dissipation of mode waters and the effects of eddies are important subjects of future studies. Ocean University of China just completed a field experiment immediately south of the winter mean outcrop line of the STMW core density southeast of Japan (*Xie,* 2013).

The results from the analysis of the field observations will shed light on eddy subduction and dissipation processes.

Appendix

Relationship between the potential vorticity of the subducted fluid (Q) and the net subduction of the water mass (M)

The Potential Vorticity (PV) in the ventilation regime may be defined in terms of fluid leaving the mixed layer and entering the stratified thermocline (Fig. A1); see the discussion of *Williams* [1989, 1991]. The PV of water subducted at the base of the mixed layer is expressed as

$$Q = -\frac{f}{\rho_0}\frac{\Delta\rho/\Delta t}{\Delta z/\Delta t} = \frac{f}{\rho_0}\frac{\dfrac{\partial\rho_h}{\partial t} + \mathbf{u}_h\cdot\nabla\rho_h}{-(\dfrac{\partial h}{\partial t} + \mathbf{u}_h\cdot\nabla h + w_h)}, \qquad \text{(A1)}$$

where ρ_h is the mixed layer density, h the MLD, $\mathbf{u}_h$ and w_h are the horizontal and vertical velocities at the base of the mixed layer, respectively, and ∇ is the horizontal differential operator. The water acquires low Q through (i) *an increase* in the subudction rate, $S = -(\frac{\partial h}{\partial t} + \mathbf{u}_h\cdot\nabla h + w_h)$, or (ii) *a decrease* in the rate of mixed layer warming, $\frac{\partial\rho_h}{\partial t}$, or cross-isopycnal flow, $\mathbf{u}_h\cdot\nabla\rho_h$.

Following *Marshall* [1997], the net subduction of the water mass (M) of a density range $\sigma_1 \leqslant \sigma < \sigma_2$ is given by the local subduction rate S multiplied by spacing, ΔA, between the two bounding outcrops, σ_1 and σ_2

$$M = S\Delta A. \qquad \text{(A2)}$$

The outcrop area bounding the subducted water mass, ΔA, is inversely proportional to the downstream gradient of the mixed layer density, $\frac{\mathbf{u}_h\cdot\nabla\rho_h}{U_h}$, where U_h is the horizontal current speed (Fig. A1). Eq. A1 can be recast as

$$Q \propto \frac{f}{\rho_0}\left(\frac{\partial \rho}{\partial t}\Delta A + U_h \Delta\rho\right)\frac{1}{S\Delta A} = \frac{f}{\rho_0}\left(\frac{\partial \rho}{\partial t}\Delta A + U_h \Delta\rho\right)\frac{1}{M}, \qquad \text{(A3)}$$

where $\Delta\rho = \sigma_2 - \sigma_1$. Thus M is related to potential vorticity at the time of subduction. Subducted water acquires low PV in the case of large subduction (M).

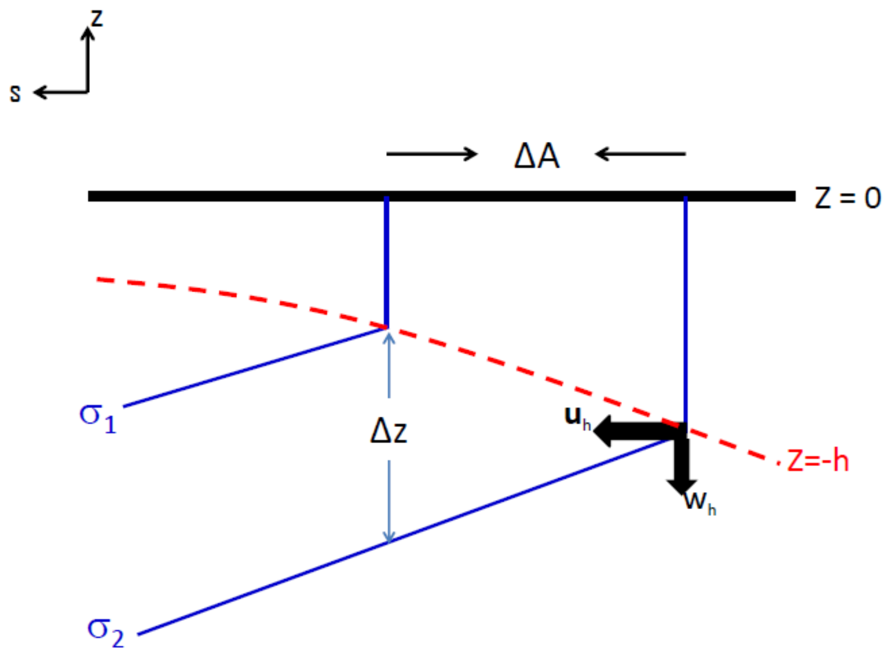

FIG. A1. Schematic diagram showing water parcels subducted from the mixed layer ($z = -h$) within a density range $\sigma_1 \leqslant \sigma < \sigma_2$. The horizontal coordinate is aligned parallel to the horizontal flow. The blue solid lines represent isopycnals and the red dashed line is the base of the mixed layer. The area over which the water mass is outcropped at the sea surface, ΔA, is inversely proportional to the downstream mixed-layer density gradient $\frac{\mathbf{u}_h \cdot \nabla \rho_h}{U_h}$.

Acknowledgements

We wish to thank Elena Yulaeva (SIO) for helping set up POPL. She also ran the POPH simulation and extracted the regional POPH output used in this study. This work was supported by the National Basic Research Program of China (2012CB955602), the China Scholarship Council, the U.S. National Science Foundation (0854365 for JLM), and the Natural Science Foundation of China (41176006 and 41221063). JLM was also supported by USDOE Office of Science Climate Modeling Programs via a Los Alamos National Laboratory subcontract. Computational resources for the POP model runs were provided by NSF resource grants TG- OCE110013 and TG-OCE130010. POPH output is available at the National Institute for Computational Sciences (NICS).

References

AVISO, (2008), SSALTO/DUACS user handbook: (M)SLA and (M)ADT near-real time and delayed time products. Version 1, Revision 9, CLS, 39 pp.

Bates, N.R., A.C. Pequignet, R.J. Johnson, and N. Gruber (2002), A variable sink for atmospheric CO_2 in subtropical mode water of the North Atlantic Ocean. *Nature,* **420**, 489–493.

Bingham, F. M. (1992), The formation and spreading of subtropical mode water in the North Pacific. *J. Geophys. Res.,* **97,** 11 177–11 189.

Cronin, M. F., C. Meinig, C. L. Sabine, H. Ichikawa, and H. Tomita (2008), Surface mooring network in the Kuroshio Extension. *Systems Journal, IEEE*, **2(3)**, 424-430.

Cushman-Roisin, B. (1987), Subduction. *Dynamics of the Oceanic Surface Mixed Layer*, P. Muller and D. Henderson, Eds., Hawaii Institute of Geophysics Special, 181–196.

Danabasoglu, G., S. C. Bates, B. P. Briegleb, S. R. Jayne, M. Jochum, W. G. Large, S. Peacock, and S. G. Yeager (2012), The CCSM4 ocean component, *J. Climate*, *25*, 1361–1389.

Ebuchi, N., and K. Hanawa (2000), Mesoscale eddies observed by TOLEX-ADCP and TOPEX/Poseidon altimeter in the kuroshio recirculation region south of Japan. *J. Oceanogr.,* **56**, 43-57.

Gent, P. R., and J. C. McWilliams (1990), Isopycnal mixing in ocean circulation models. *J. Phys. Oceanogr.,* **20**(1), 150-155.

Guo, X., H. Hukuda, Y. Miyazawa, and T. Yamagata (2003), A triply nested ocean model for simulating the Kuroshio—Roles of Horizontal Resolution on JEBAR. *J. Phys. Oceanogr.*, **33**, 146–169.

Hanawa, K. (1987), Interannual variations in the wintertime outcrop area of Subtropical Mode Water in the western North Pacific Ocean. *Atmos.–Ocean,* **25,** 358–374.

Hanawa, K., and L. D. Talley (2001), "4. Mode waters." *International Geophysics* **77**: 373-386.

Huang, R. X., and B. Qiu (1994), Three-dimensional structure of the wind-driven circulation in the subtropical North Pacific. *J. Phys. Oceanogr.*, **24**, 1608–1622.

Kobashi, F., H. Mitsudera, and S.-P. Xie (2006), Three subtropical fronts in the North Pacific: Observational evidence for mode water-induced subsurface frontogensis. *J. Geophys. Res.-Oceans*, **111**, C09033, doi:10.1029/2006JC003479.

Kouketsu S., H. Tomita, E., Oka S. Hosoda, T. Kobayashi, and K. Sato (2011), The role of meso-scale eddies in mixed layer deepening and mode water formation in the western North Pacific. *J. Oceanogr.,* 2012, **68**(1): 63-77.

Kubokawa, A. (1997), A two-level model of subtropical gyre and subtropical countercurrent. *J. Phys. Oceanogr.,* **53,** 231-244.

Kwon, E.Y., S. M. Downes, J. L. Sarmiento, R. Farneti, and C. Deutsch (2013), Role of the Seasonal Cycle in the Subduction Rates of Upper–Southern Ocean Waters. *J. Phys. Oceanogr.*, **43**, 1096–1113.

Ladd, C., and L. Thompson (2001), Water Mass Formation in an Isopycnal Model of the North Pacific. *J. Phys. Oceanogr.* **31**, 1517-1537.

Large, W.G., J.C. McWilliams, and S.C. Doney (1994), Oceanic vertical mixing: a review and a model with nonlocal boundary layer parameterization. *Rev. Geophys.* **32**, 363-403.

Large, W.G., and S. G. Yeager (2009), The climatology of an interannually-varying air-sea flux data set. *Clim. Dyn.*, **33**, 31-364.

Liu C., and P. Li (2013), The impact of meso-scale eddies on the Subtropical Mode Water in the western North Pacific, *J. Ocean Univ. China*, **12**, 2, 230.

Maltrud, M., F. Bryan, and S. Peacock (2010), Boundary impulse response functions in a century-long eddying global ocean simulation. *Environ. Fluid Mech.* **10**(1-2), 275-295. doi:10.1007/s10652-009-9154-3.

Marshall, D. (1997), Subduction of water masses in an eddying ocean. *J. Marine Res.*, **55**(2): 201-222.

Nishikawa, S., H. Tsujino, K. Sakamoto, and H. Nakano (2010), Effects of Mesoscale Eddies on Subduction and Distribution of Subtropical Mode Water in an Eddy-Resolving OGCM of the Western North Pacific. *J. Phys. Oceanogr.*, **40**, 1748–1765.

Oka E., K. Toyama, and T. Suga (2009), Subduction of North Pacific central mode water associated with subsurface mesoscale eddy. Geophysical Research Letters, 36, L08607, doi:10.1029/2009GL037540.

Oka, E., and B. Qiu (2012), Progress of North Pacific mode water research in the past decade. *J. Oceanogr.,* **68**, 5-20.

Oka, E., and T. Suga (2003), Formation region of North Pacific Subtropical Mode Water in the late winter of 2003. *Geophysical Research Letters*, **30**(23), 2205, doi:10.1029/2003GL018581.

Oka, E., and T. Suga (2005), Differential formation and circulation of North Pacific Central Mode Water. *Journal of Physical Oceanography*, **35**, 1997-2011.

Pan, A., and Q. Liu (2005), Mesoscale eddy effects on the wintertime vertical mixing in the formation region of the North Pacific Subtropical Mode Water, *Chinese Science Bulletin*, **50**(17), P.1949-1956.

Qiu B., and R. X. Huang (1995), Ventilation of the North Atlantic and North Pacific: subduction versus obduction. *J. Phys. Oceanogr.* **25**:2374-2390.

Qiu, B., and S. Chen (2006), Decadal variability in the formation of the North Pacific Subtropical Mode Water: Oceanic versus atmospheric control. *J. Phys. Oceanogr.*, **36**, 1365-1380.

Qiu, B., S. Chen, and P. Hacker (2007), Effect of mesoscale eddies on Subtropical Mode Water variability from the Kuroshio Extension System Study (KESS). *J. Phys. Oceanogr.*, **37**, 982-1000.

Qu, T., S.-P. Xie, H. Mitsudera, and A. Ishida (2002), Subduction of the North Pacific Mode Waters in a global high-resolution GCM. *J. Phys. Oceanogr.*, **32**, 746–763.

Rio, M. H., S. Guinehut, and G. Larnicol (2011), New CNES-CLS09 global mean dynamic topography computed from the combination of GRACE data, altimetry, and in situ measurements, *J. Geophys. Res.*, **116**, C07018, doi:10.1029/2010JC006505.

Roemmich, D., and J. Gilson (2009), The 2004-2008 mean and annual cycle of temperature, salinity, and steric height in the global ocean from the Argo Program. *Progress in Oceanography*, **82,** 81-100.

Sasaki, H., M. Nonaka, Y. Masumoto, Y. Sasai, H. Uehara, and H. Sakuma (2008), An eddy-resolving hindcast simulation of the quasiglobal ocean from 1950 to 2003 on the Earth Simulator. In High Resolution Numerical Modelling of the Atmosphere and Ocean, *K. Hamilton and W. Ohfuchi (eds.)*, chapter 10, pp. 157–185, Springer, New York.

Smith, R. D., M. E. Maltrud, F. O. Bryan, and M. W. Hecht (2000), Numerical simulation of the North Atlantic Ocean at 1/10°. *J. Phys. Oceanogr.,* **30**, 1532–1561.

Suga, T., and K. Hanawa (1990), The mixed-layer climatology in the northwestern part of the North Pacific subtropical gyre and the formation area of Subtropical Mode Water. *J. Mar. Res.,* **48,** 543–566.

Suga, T., K. Motoki, Y. Aoki, and A. M. Macdonald (2004), The North Pacific climatology of winter mixed layer and mode waters. *J. Phys. Oceanogr.*, **34**, 3–22.

Suga, T., Y. Aoki, H. Saito, and K. Hanawa (2008), Ventilation of the North Pacific subtropical pycnocline and mode water formation. *Prog. Oceanogr.,* **77**, 285-297.

Taguchi, B., S.-P. Xie, N. Schneider, M. Nonaka, H. Sasaki, and Y. Sasai (2007), Decadal variability of the Kuroshio Extension: Observations and an eddy-resolving model hindcast. *J. Climate*, **20**, 2357-2377.

Uehara, H., T. Suga, K. Hanawa, and N. Shikama (2003), A role of eddies in formation and transport of North Pacific Subtropi- cal Mode Water. *Geophys. Res. Lett.*, **30**, 1705, doi:10.1029/2003GL017542.

Williams, R.G. (1989), The influence of air-sea interaction on the ventilated thermocline. *J. Phys. Oceanogr .,* **19**:1255-1267.

Williams, R.G. (1991), The role of the mixed layer in setting the potential vorticity of the main thermocline. *J. Phys. Oceanogr .,* **21**:1803-1814.

Xie, S.-P. (2013), Advancing climate dynamics toward reliable regional climate projections, *J. Ocean Univ. China*, *12*, 191-200.

Xie, S.-P., T. Kunitani, A. Kubokawa, M. Nonaka, and S. Hosoda (2000), Interdecadal thermocline variability in the North Pacific for 1958-1997: A GCM simulation. *J. Phys. Oceanogr.*, **30**, 2798-2813.

Xie, S.-P., L. Xu, Q. Liu, and F. Kobashi (2011), Dynamical Role of Mode Water Ventilation in Decadal Variability in the Central Subtropical Gyre of the North Pacific. *J. Climate.*, **24**, 1212-1225.

Xu, L.X., S.-P. Xie, Q. Liu, and F. Kobashi (2012a), Response of the North Pacific Subtropical Countercurrent and its variability to global warming. *J. Oceanogr.*, **68**, 127-137, doi:10.1007/s10872-011-0031-6.

Xu, L. X., S.-P. Xie, and Q. Liu (2012b). Mode water ventilation and subtropical countercurrent over the North Pacific in CMIP5 simulations and future projections. *J. Geophys. Res.-Oceans*, **117**, C12009, doi:10.1029/2012JC008377.

Table 1. List of properties for STMW and CMW, includes the core layer density, density range, total subduction (M_{total}) and its components (M_{mean} and M_{eddy}) integrated for the entire density range for observations, OFES, POPH, and POPL.

Data	Core layer (σ_θ)	Density range (σ_θ)	M_{total} (Sv)	M_{mean} (Sv)	M_{eddy} (Sv)
Obs.					
STMW	25.3	24.9~25.5	8.99	4.02	4.98
CMW	26.0	25.7~26.6	7.29	3.27	4.02
OFES					
STMW	25.3	25.2~25.6	13.10	2.77	10.33
CMW	26.2	26.0~26.4	11.78	4.37	7.42
POPH					
STMW	25.0	24.8~25.3	11.24	3.11	8.13
CMW	25.9	25.9~26.3	8.33	3.51	4.82
POPL					
STMW	25.4	25.3~25.8	4.31	3.74	0.57
CMW	26.0	26.0~26.4	6.20	5.81	0.39

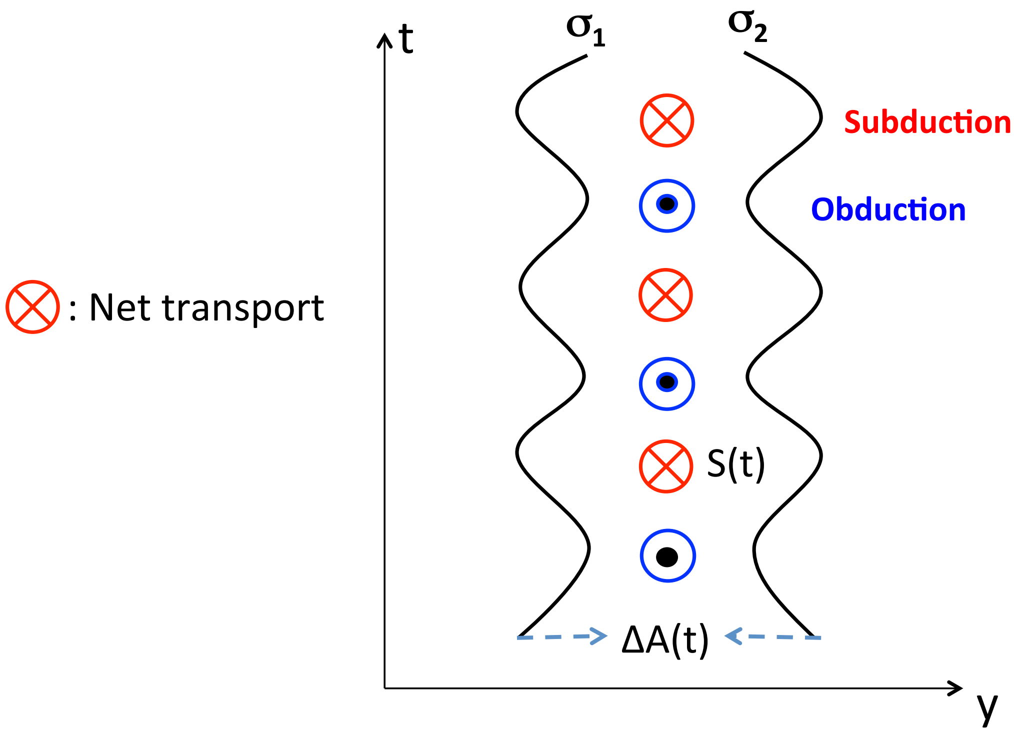

FIG. 1. Schematic illustrates the eddy subduction process, resulting from the correlation between the subduction/ obduction rate *S(t)* and the outcrop area $\Delta A(t)$. The solid lines represent two isopycnals, σ_1 and σ_2, defining the upper and lower bounds of a particular water mass. The outcrop area is relatively larger during the subduction period compared with the obduction period, leading to the net downward volume transport. The net subduction can remain finite even when the Eulerian-mean subduction rate $\overline{S}$ is zero. Adapted from *Marshall* [1997].

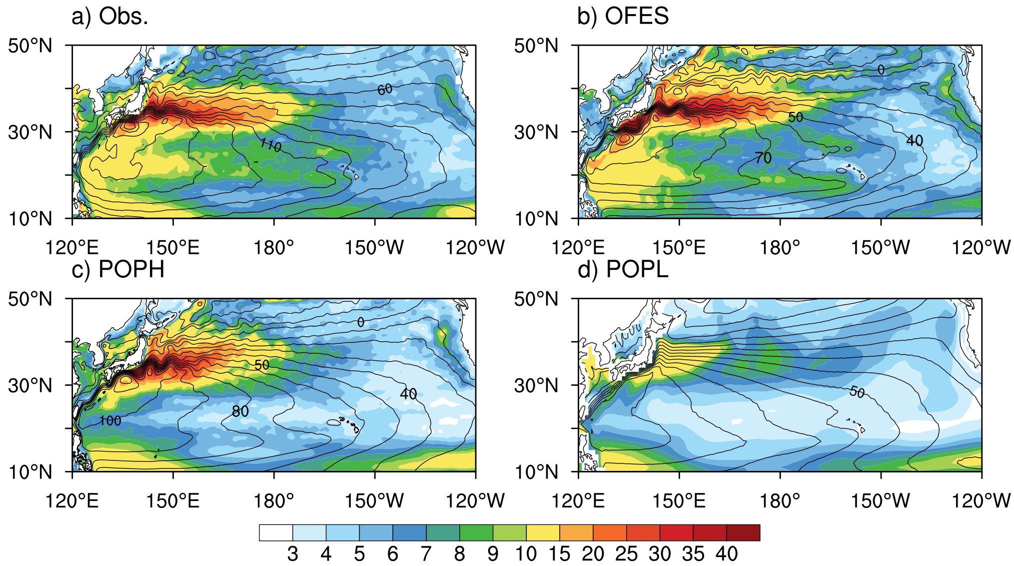

FIG. 2. Mean (contours in 10 *cm* intervals) and standard deviation (shaded in *cm*) of SSH from a) observations (Obs.), b) the Ocean Model for the Earth Simulator (OFES), c) the Parallel Ocean Program with High-resolution (POPH), and d) the Parallel Ocean Program with Low-resolution (POPL).

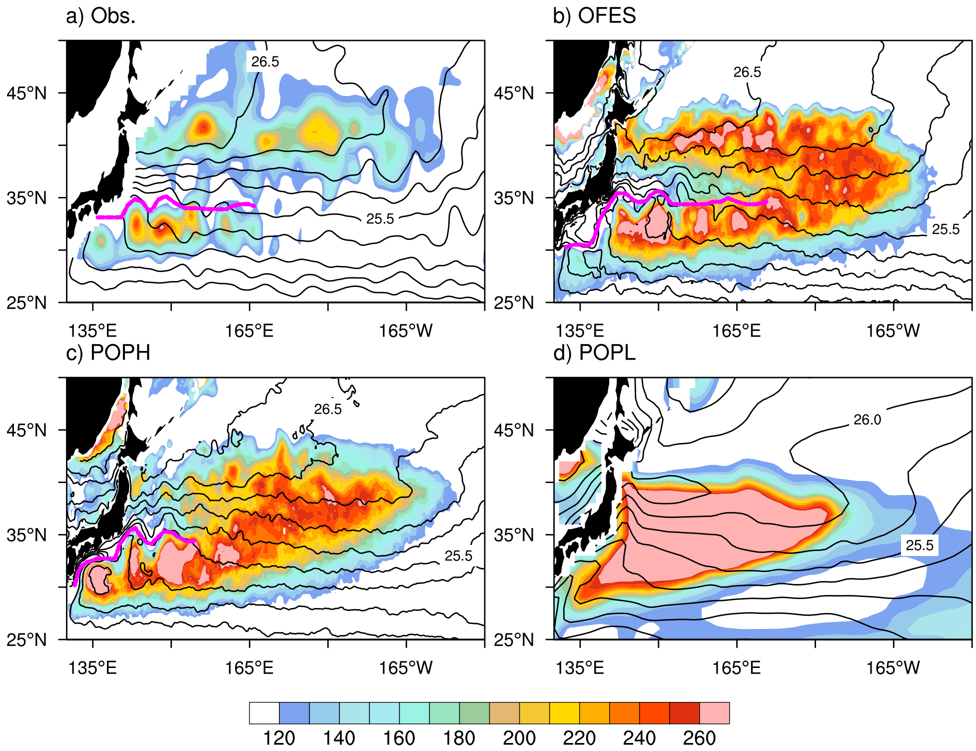

FIG. 3. March mean MLD (color shade in *m*) and surface density (black contours in 0.25 $kg\ m^{-3}$ intervals) for a) Obs., b) OFES, c) POPH, and d) POPL. The KE jet is denoted by a thick magenta line for a), b) and c). Note that there is no magenta line in d), because POPL could not simulate the KE jet.

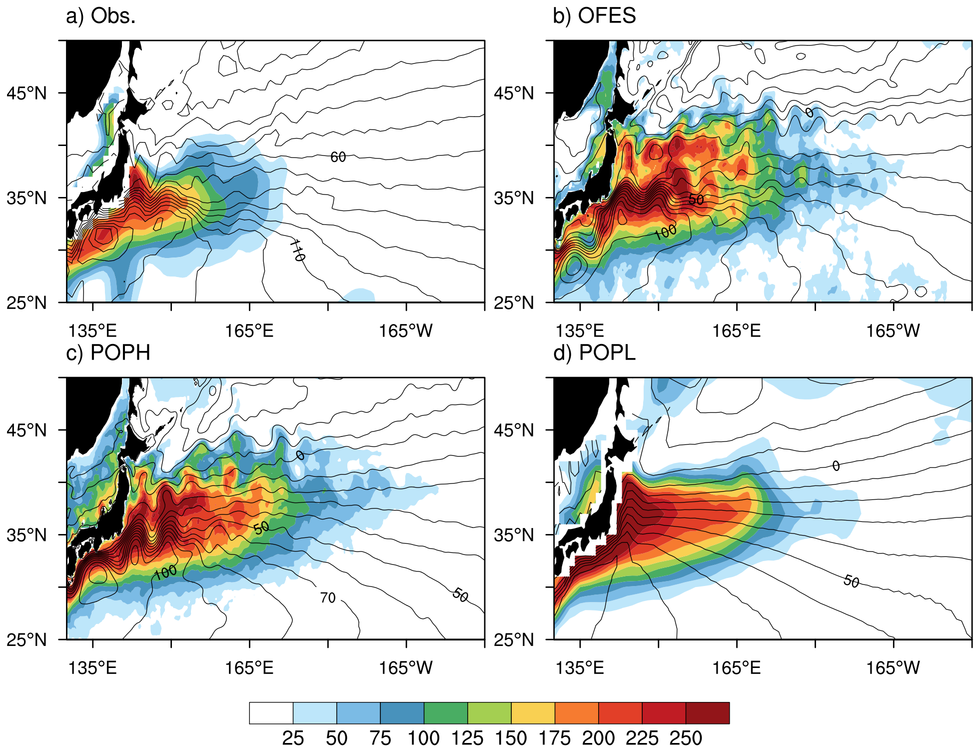

FIG. 4. March mean net surface heat flux (shaded in $W\ m^{-2}$, positive upward) and mean SSH (black contours in 10 *cm* intervals) for a) Obs. from NCEP reanalysis, b) OFES, c) POPH, and d) POPL.

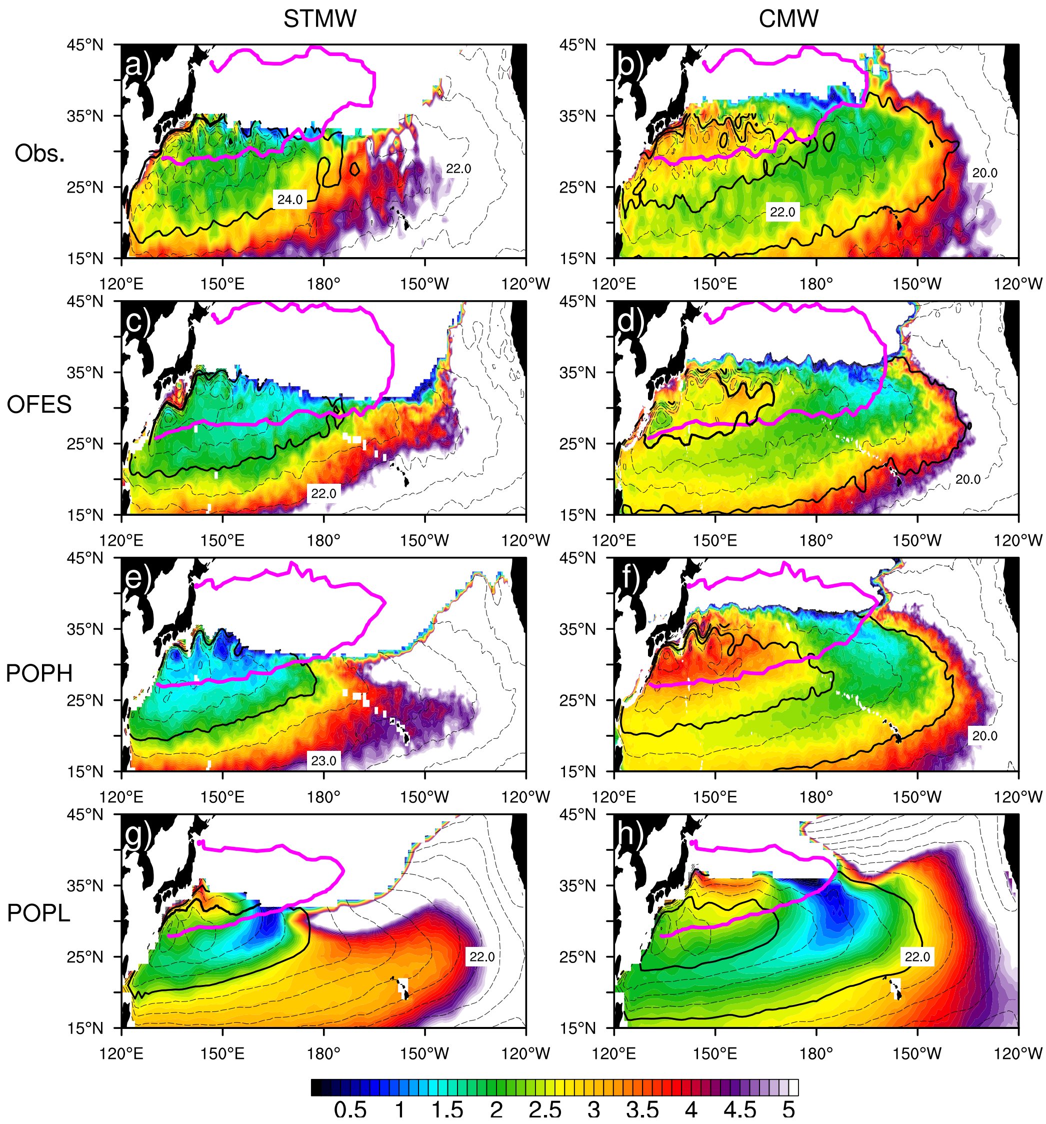

FIG. 5. March mean PV (shaded in 10^{-10} m^{-1} s^{-1}) and acceleration potential (black contours at 1.0 m^2 s^{-2} intervals) on the core layers (see Table 1) of STMW (left panels) and CMW (right panels). The top panels are for Obs., second from the top for OFES, third for POPH and the bottom for POPL. The 100 *m* (150 *m*) MLD contour is plotted in thick magenta line to mark the MLD front for Obs. (OFES, POPH and POPL).

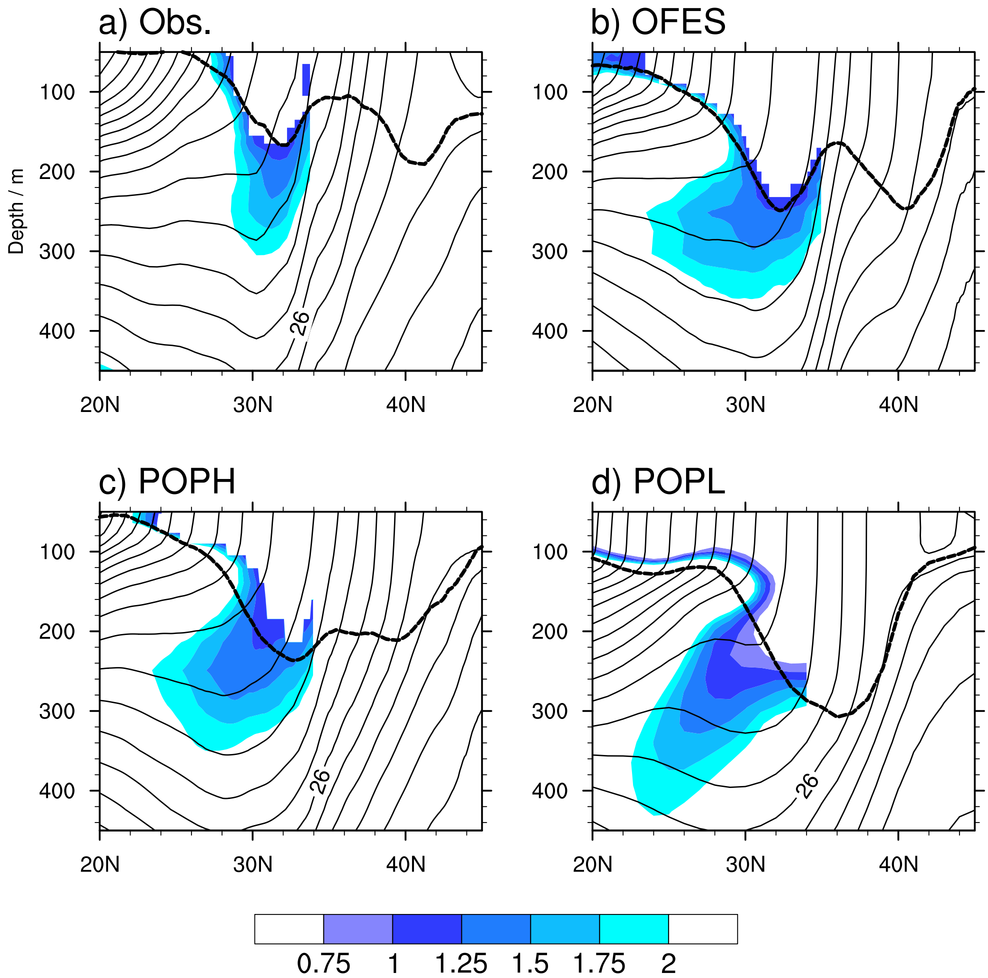

FIG. 6. March zonal mean (140-180°E) sections of potential density (black contours in 0.2 $kg\ m^{-3}$ intervals) and MLD (dashed black line) and PV (shaded in $10^{-10}\ m^{-1}\ s^{-1}$) for a) Obs., b) OFES, c) POPH, and d) POPL.

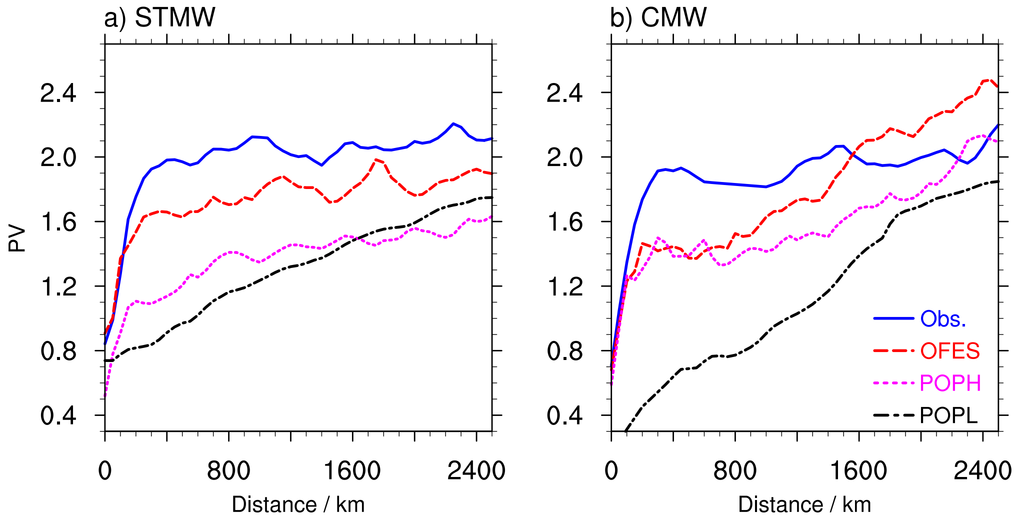

FIG. 7. PV (10^{-10} m^{-1} s^{-1}) dissipation along mean trajectory of the low PV tongue for the core layers of a) STMW and b) CMW. The mean trajectory of the low PV tongue is defined as between the streamlines (solid lines in Fig. 5) which bound the low PV water. The path is different among models and the two kinds of mode waters. The x-axis is the distance from the mode water's subduction sites. The solid blue line is for Obs., the dashed red line is for OFES, the magenta dotted line for POPH, and the black dashed-dot line is for POPL (legend at the right-bottom).

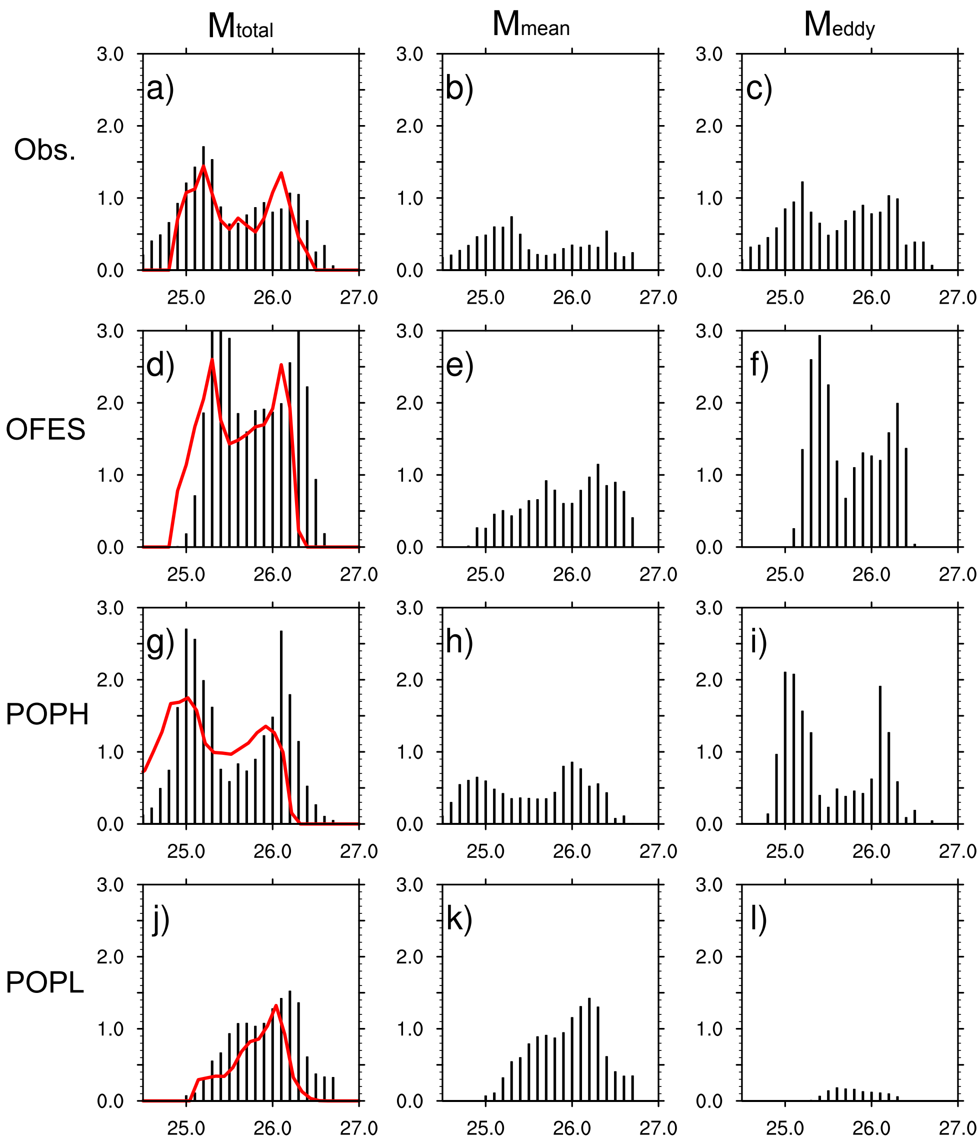

FIG. 8 Total subduction (M_{total}) and its components (M_{mean} and M_{eddy}) for each density class (Sv in black bars). The calculation domain is 135°E-155°W, 25°-45°N. Left panels are for the total subduction (M_{total}), middle panels for the mean subduction (M_{mean}), and right panels for the eddy subduction (M_{eddy}). The upper panels are for Obs., second from the top for OFES, third for POPH and the bottom for POPL. The red curve on the left panels is the total volume (10^{14} m^3) of the low PV water ($< 1.5 \times 10^{-10}$ m^{-1} s^{-1}) for each density class over the North Pacific (120°E-140°W, 20-40°N).

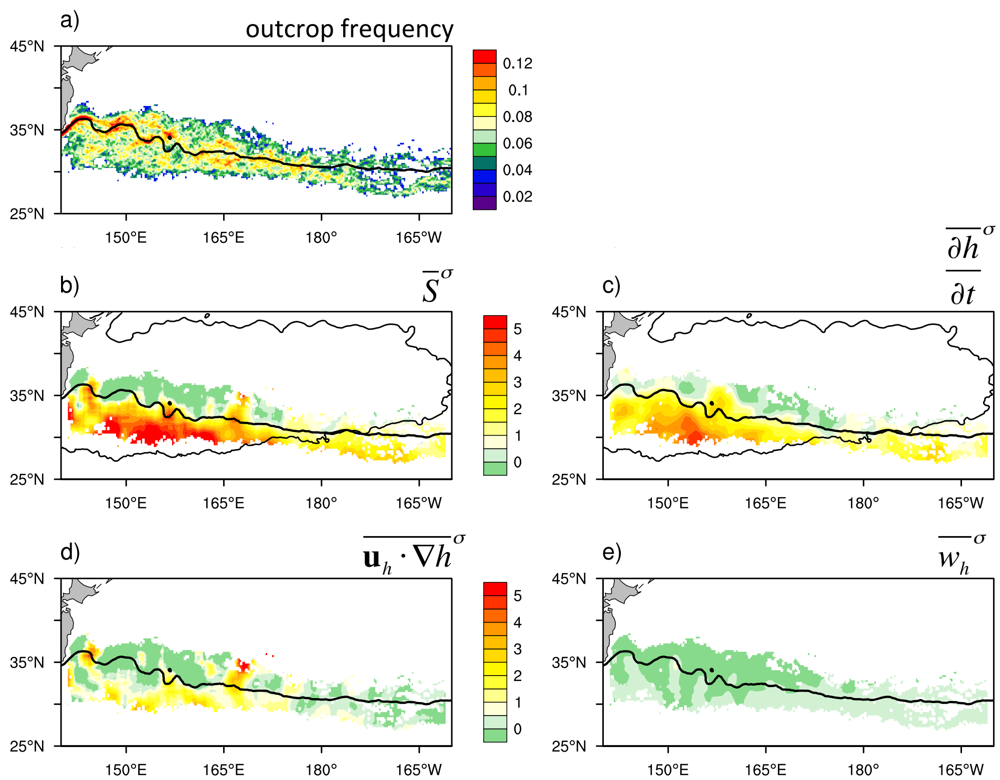

FIG. 9. a) Outcrop frequency of the 25.3 ±0.05 σ_θ layer based on the OFES 3-day outputs in March from 1994 to 2007. The lower four panels are the isopycnal subduction rate and its components (positive downward, shaded in10^{-5} *m/s*): b) total subduction rate $\overline{S}^{\sigma}$, c) temporal induction ($\overline{\frac{\partial h}{\partial t}}^{\sigma}$), d) lateral induction ($\overline{\mathbf{u}_h \cdot \nabla h}^{\sigma}$), and e) vertical pumping ($\overline{w_h}^{\sigma}$). The superscript σ indicates that it is averaged for a given isopycnal layer, distinct form the Eulerian mean. The mean 25.3 σ_θ outcrop line is denoted in thick black solid line, and the March mean MLD front in black solid line (b and c).

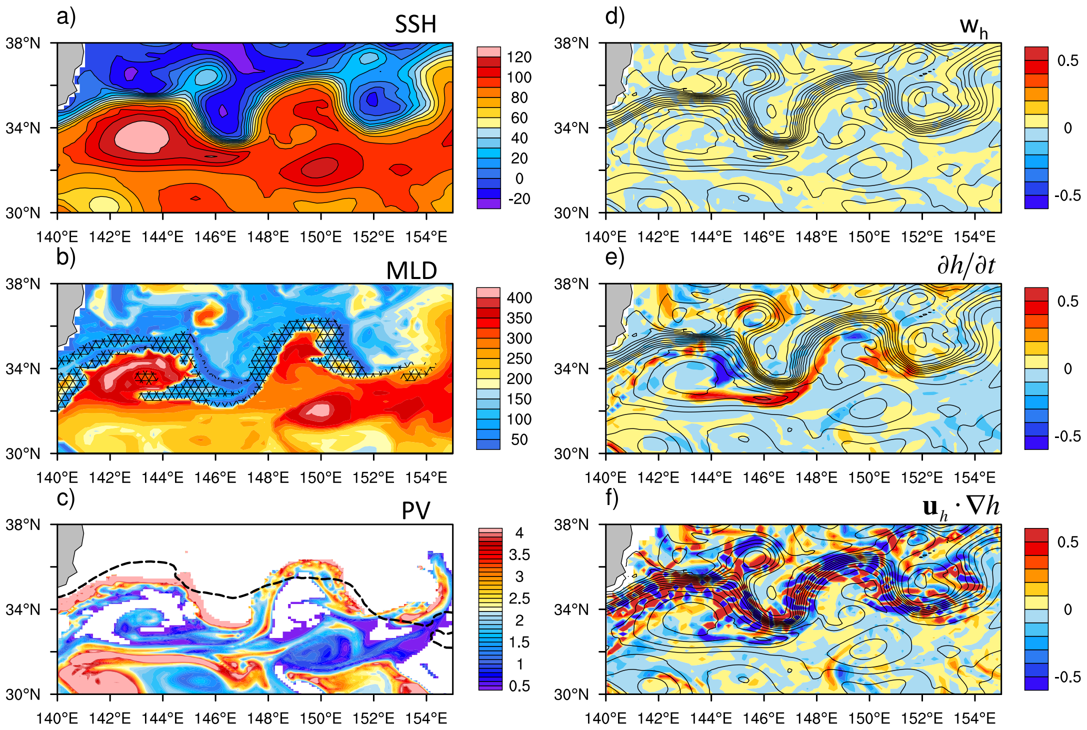

FIG. 10. A snapshot from OFES on March 26, 2000. The left hand panels include a) SSH (shaded in *cm*, the reds/blues are for the anticyclonic/cyclonic eddies, respectively), b) MLD (shaded in *m*), with the outcrop area of 25.3 ± 0.05 σ_θ superimposed in black hatched patterns, and c) PV (shaded in 10^{-10} m^{-1} s^{-1}) on 25.3 σ_θ, with the March mean 25.3 σ_θ outcrop line superimposed in black dashed line. The right hand panels show the three components of the instantaneous subduction rate (positive downward, shaded in 10^{-3} *m/s*): d) vertical pumping w_h, e) temporal induction $\frac{\partial h}{\partial t}$, and f) lateral induction $\mathbf{u}_h \cdot \nabla h$. The SSH is superimposed in d-f as black contours in 10 *cm* intervals.

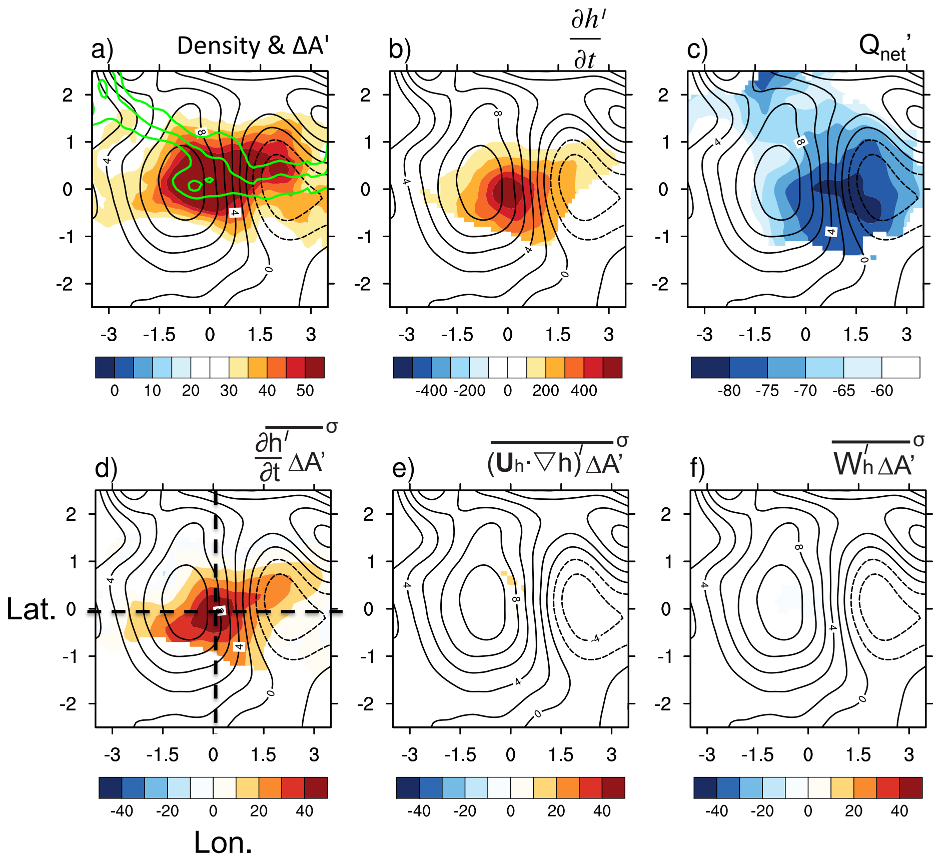

FIG. 11. Composite of eddy subduction process based on OFES 3-day outputs in March from 1994 to 2007. The center locations are where the maximum eddy subduction takes place. a) Outcrop area anomalies $\Delta A'$ (km^2; outcrop frequency of the 25.3±0.05 σ_θ layer times the grid bin area), together with surface density contours of 25.25, 25.30 and 25.35 σ_θ in green; b) $\frac{\partial h'}{\partial t}$ (positive downward in 10^{-6} *m/s* intervals); c) net heat flux anomalies Q_{net}' (W/m^2, negative downward). Three components of the isopycnal subduction (Subduction rate times outcrop area within 25.3±0.05 σ_θ; positive downward in 10^{-3} *Sv*): d) MLD tendency term $\overline{\frac{\partial h'}{\partial t}\Delta A'}^{\sigma}$; e) lateral induction $\overline{(\mathbf{u}_h \cdot \nabla h)'\Delta A'}^{\sigma}$; and f) vertical pumping $\overline{w_h'\Delta A'}^{\sigma}$. Only values passing 95% confidence level are shown. The SSH anomalies (black contours at 2 *cm* intervals; negative values dashed) are superimposed. The thick black dashed lines in d) indicate the positions for the composite transections in Fig. 12.

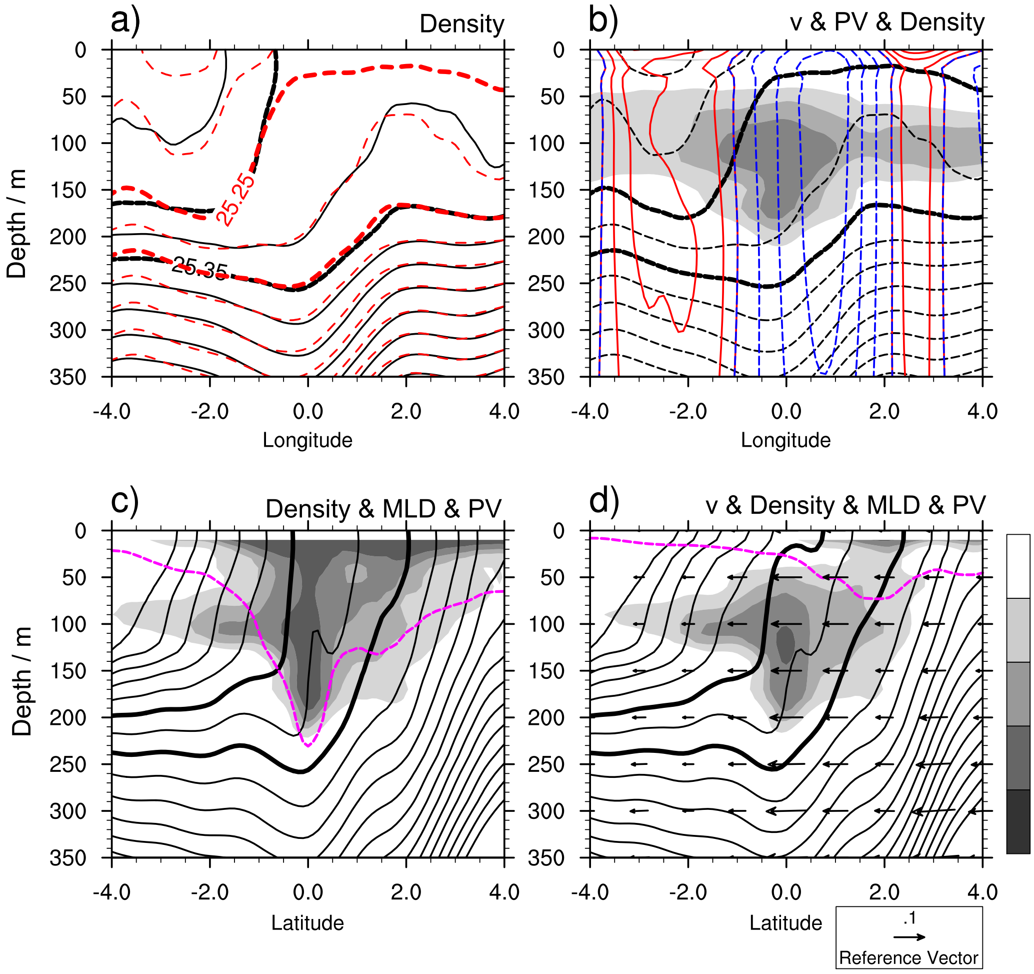

FIG. 12. Zonal (a-b) and meridional (c-d) vertical sections of the composite as shown in Fig. 11d. The zonal sections are for a) potential density (black contours at 0.05 $kg\ m^{-3}$ intervals), with the 3-day lagged field superimposed in red dashed contours (the 25.25 and 25.35 σ_θ contour thickened); and b) low PV (shaded in $0.1\times10^{-10}\ m^{-1}\ s^{-1}$ intervals), meridional velocity (red contours for northward flow and blue dashed contours for southward flow), and potential density (the 25.25 and 25.35 σ_θ contours thickened). The meridional sections are for c) low PV (gray shaded), MLD (magenta line), and potential density (black contours, the 25.25 and 25.35 σ_θ contours are highlighted in thick line), and d) as in c) with the 3-day lagged values, the southward flow is shown by vectors at *m/s*.

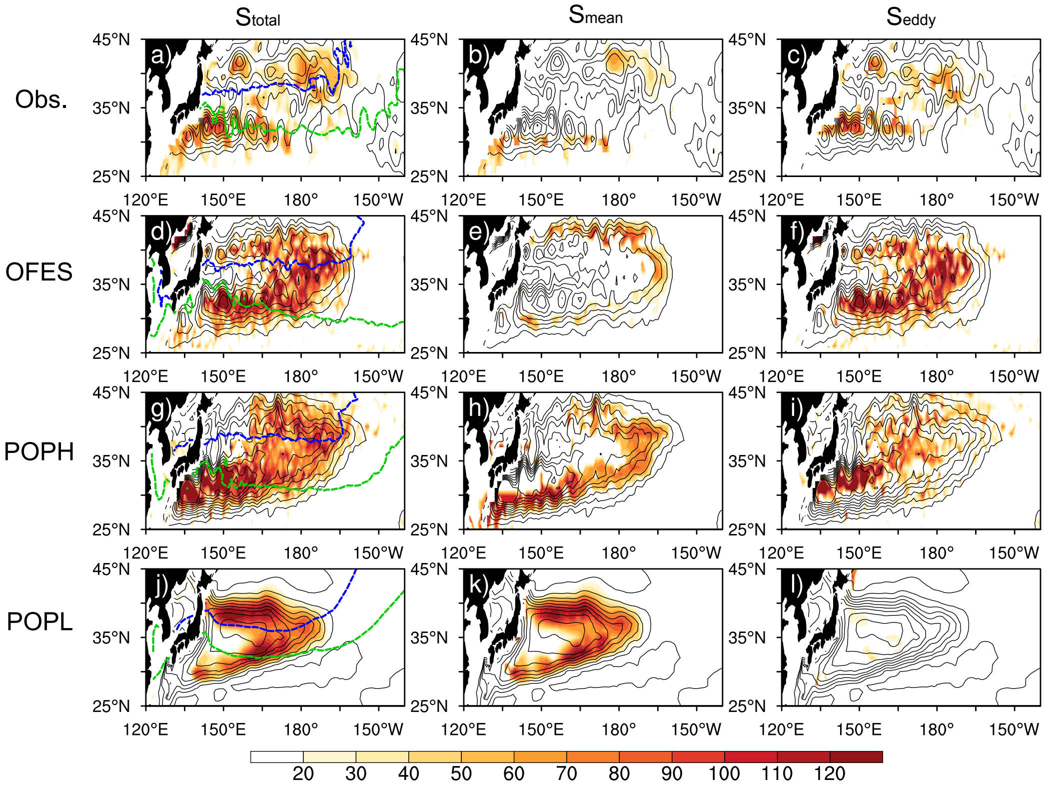

FIG. 13. The annual subduction rate S_{total} (positive downward, shaded in *m/yr*) based on high-frequency model outputs (left panels) and its constituents of the mean subduction S_{mean} (middle panel) and eddy subduction S_{eddy} (right panel). The top panels are for Obs., second from the top for OFES, third for POPH and bottom for POPL. Only the positive values are plotted. The March climatology MLD (>100 *m*) is superimposed in black contours at 25 *m* intervals. The outcrops for the core density of STMW (green line) and CMW (blue line) are denoted on the left hand panels.

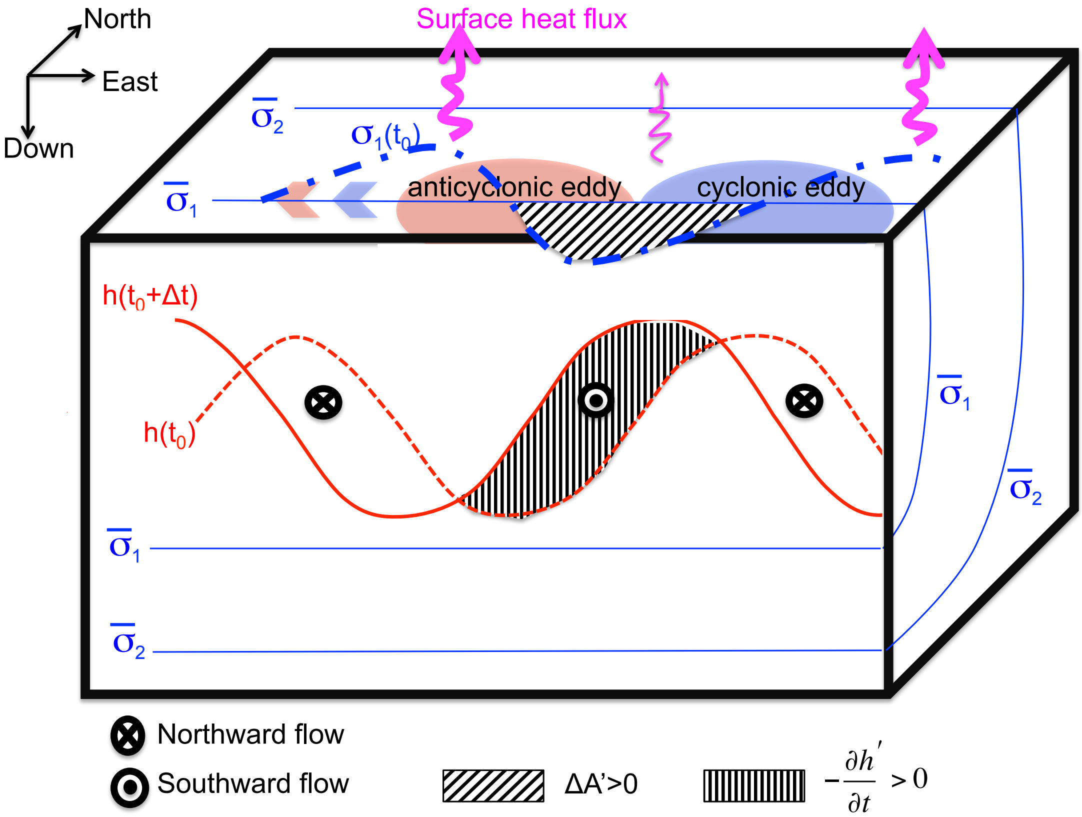

FIG. 14. Schematic illustrates the eddy subduction process. With an anticyclonic eddy to the west and a cyclonic eddy to the east, the instantaneous outcrop line $\sigma_1(t_0)$ meanders south, where the isopycnal is occasionally exposed to the atmosphere by eddies. This increasing outcrop area is collocated with the temporal shoaling of MLD from the red dashed line $h(t_0)$ to the solid red line $h(t_0 + \Delta t)$ as the eddy pair travels westward. The isopycnal σ_1 is soon to be sheltered from the surface as the MLD shoals in time, forming the mode water. The cross-correlation between the temporal shoaling of the MLD, $\frac{\partial h'}{\partial t}$, and the increasing outcrop area, $\Delta A'$, intensifies subduction. The southward eddy flow then carries the subducted water mass into the thermocline.